RSC Advances

PAPER

View Article Online
View Journal | View Issue

Cite this: *RSC Adv.*, 2026, **16**, 22293

MoO_2/biochar catalysts for oxidative desulfurization toward ultra-low sulfur diesel *via* carbothermal reduction of pistachio shell waste

Barham S. Ahmed, * Luqman O. Hamasalih and Abdul-Salam R. Karim

The requirement for ultra-low-sulfur diesel (ULSD) quality necessitates the use of heterogeneous catalysts with high oxidative desulfurization (ODS) activity, which are also robust and inexpensive to produce. In this work, we describe a new type of molybdenum-functionalized biochar catalyst (MoPSBC) prepared from pistachio shell (PS) agricultural waste *via* impregnation followed by carbothermal reduction, providing a novel means of simultaneously valorizing agricultural waste and preparing well-dispersed monoclinic MoO_2 nanoparticles with a well-developed carbon framework, as evidenced by SEM analysis. Physicochemical characterization using XRD, FTIR spectroscopy, SEM-EDX, and DSC revealed that 10 wt% Mo is the optimal loading, maximizing active-site availability while maintaining high metal–support interactions and dispersion efficiency. Under optimal reaction conditions (1 h, 70 °C, and H_2O_2/S molar ratio = 6), the 15MoPSBC catalyst exhibited high DBT conversion (>99.3%) in 10 000 ppm DBT model fuel. When tested on real gas oil with 1715 ppm sulfur, formic acid-promoted 10MoPSBCF, where formic acid acts as an *in situ* oxidant precursor to boost the Mo active site turnover, reduced the total sulfur content to about 89 ppm (94.6% sulfur removal), showing practical applicability to real-world feedstocks. Mechanistic studies revealed that the reversible Mo^{4+}/Mo^{6+} redox cycle produced highly electrophilic oxoperoxo-molybdenum species as primary active sites, while the graphitic biochar surface enabled π–π stacking interactions for refractory dibenzothiophene (DBT) sequestration, as revealed by FTIR and SEM characterization. Kinetic studies validated pseudo-first-order kinetics with respect to the concentration of DBT. These results demonstrate the potential of MoPSBC as a cost-effective, biomass-derived catalytic platform for advanced fuel purification, providing a scalable solution for ULSD production.

Received 13th March 2026
Accepted 13th April 2026

DOI: 10.1039/d6ra02134d

rsc.li/rsc-advances

1 Introduction

The global energy landscape continues to rely heavily on fossil fuels, particularly gasoline and diesel, despite the growing environmental worries and the transition towards renewable energies.[1,2] During this transition, advanced energy storage devices have emerged as significant contributors to decarbonization efforts;[3,4] yet, liquid fuels remain indispensable for heavy transport and industries. The main obstacle to fossil fuel use is that the organosulfur compounds in these fuels release sulfur oxides (SO_x) during combustion, which lead to acid rain, equipment damage and air contamination.[5] Additionally, these organosulfur compounds can poison catalysts and other advanced energy conversion devices.[6] Consequently, the development of effective and economically viable desulfurization technologies remains a critical priority for the petroleum refining industry and environmental protection efforts.[7]

Traditional hydrodesulfurization (HDS) has been the predominant industrial method for sulfur removal from petroleum products.[8] However, HDS requires high hydrogen pressure, elevated temperatures, and large reactors, making it economically expensive, particularly for deep desulfurization. Moreover, HDS does not react with refractory sulfur compounds, such as dibenzothiophene and 4,6-dimethyldibenzothiophene.[9–13] Therefore, the development of more efficient and environmentally friendly desulfurization approaches is essential. Among these, oxidative desulfurization (ODS) has attracted significant research attention as a highly promising technology.[14,15]

ODS offers several advantages over traditional HDS, such as mild operating conditions (typically 30–80 °C and ambient pressure), higher selectivity for oxidation of refractory sulfur compounds, and no requirement for molecular hydrogen.[16,17] In ODS, sulfur compounds are oxidized to polar sulfones, which can be easily removed *via* extraction or adsorption.[18–20] The efficiency of ODS systems is highly dependent on the oxidizing agents used (such as organic peroxides, O_2 or H_2O_2) and, more importantly, on the catalysts used to promote the oxidation reaction.[21,22] Various catalytic materials have been investigated

Department of Chemistry, College of Science, University of Sulaimani, Qliasan Street, Sulaymaniyah City, Kurdistan Region, 46002, Iraq. E-mail: barham.sharif@univsul.edu.iq

for ODS, including deep eutectic solvents,[23] polyoxometalates,[24] ionic liquids,[25] transition-metal oxides,[26] and metal–organic frameworks.[27]

Among the transition metals, molybdenum oxide has demonstrated exceptional promise due to its versatile redox behavior, high oxygen transfer ability, and high stability under oxidative conditions.[28,29] As a transition metal, molybdenum forms various compounds, particularly molybdenum oxides (MoO_x), which exist in multiple oxidation states (mainly Mo^{4+}, Mo^{5+}, and Mo^{6+}), enabling them to undergo multiple electron-transfer reactions that are essential for catalytic oxidation reactions.[30] Moreover, molybdenum species have the ability to form peroxo-metal complexes in the presence of hydrogen peroxide, which produce highly reactive species that can efficiently oxidize organosulfur compounds.[31] Bulk MoO_x catalysts have poor dispersion and limited interfacial compatibility in biphasic oil–water systems. Aggregation also lowers the density of active sites; prevents contact between sulfur substrates, oxidants, and catalytic centers; and hinders mass transfer, reducing catalytic turnover and desulfurization efficiency.[32] Thus, rational support engineering is needed to stabilize molybdenum species and enhance interfacial mass transfer and catalytic efficiency.

Supported MoO_x catalysts have been extensively developed using porous materials, such as transition-metal oxides, Al_2O_3, SiO_2, molecular sieves, and MOFs.[33] While these supports improve metal dispersion and surface accessibility, they often suffer from limitations related to high cost, complex synthesis procedures, and limited sustainability.[34] Moreover, these conventional inorganic supports were primarily designed for hydrodesulfurization (HDS) processes operating under harsh conditions, typically involving elevated temperatures and high hydrogen pressures.

In contrast, ODS systems operate under mild conditions (30–80 °C, ambient pressure) and commonly involve biphasic oil–aqueous oxidant systems, where mass transfer at the liquid–liquid interface plays a crucial role in determining catalytic efficiency. Therefore, the selection of suitable supports that can facilitate interfacial interactions is of paramount importance. In this regard, biochar has been increasingly recognized as an attractive and sustainable support for Mo-based ODS catalysts.[35]

Biochar, derived from the pyrolysis of biomass under inert conditions,[36–38] has a distinctive set of physicochemical properties, such as high surface area, hierarchical porosity, and numerous surface functional groups.[39,40] It is an amphiphilic substance and therefore allows increased contact between the organic and aqueous phases, thus increasing interfacial mass transfer. Moreover, oxygen-containing functional groups, such as hydroxyl, carboxyl, and phenolic groups, also support strong interactions between the metal and the support, thereby facilitating the dispersion and stabilization of Mo active species and affecting their electronic structure, increasing their redox activity.[41,42]

Additionally, the presence of partially graphitized areas in biochar allows π–π interactions with aromatic sulfur compounds, enhancing their adsorption and local concentration in the vicinity of the active sites. This, together with its porous structure, helps to enhance the diffusion and catalytic turnover in biphasic systems.[43] These synergistic characteristics, coupled with its low cost, renewability and environmental compatibility, make biochar a highly appropriate support for ODS applications of Mo-based catalysts.[44] The porous nature of biochar facilitates the access of sulfur compounds to active sites, and Mo functionalization helps facilitate dispersion, prevent aggregation, and stabilize the active species, leading to high desulfurization performance in comparison to unsupported or conventional catalysts.[45,46]

The primary objective of this work is to develop a sustainable and economically viable MoO_2/biochar catalyst for the production of ultra-low sulfur diesel *via* ODS under mild conditions. PSBC was used as a support to form a catalyst with enhanced interfacial properties. Lignocellulosic carbon matrix encourages π–π interactions with aromatic sulfur compounds, thereby leading to their adsorption and allowing increased accessibility to active sites. After treatment with HNO_3 and carbothermal reduction, densely packed active sites, which are well-dispersed MoO_2 nanoparticles, were achieved. The amphiphilic support of the biochar facilitates compatibility in biphasic systems, which increases the interfacial mass transfer and total desulfurization efficiency under mild conditions.

2 Experimental

2.1. Materials and reagents

2.1.1. Raw materials and chemicals. Pistachio shells, a carbon-rich lignocellulosic waste, were collected from local sources in the Kurdistan Region of Iraq and utilized as a sustainable precursor for biochar production. The primary green oxidant used throughout the study was hydrogen peroxide (H_2O_2, 30 wt%), while nitric acid (HNO_3, 0.1 N), was utilized for the chemical activation and functionalization of the biochar support. Nitrogen gas (99.99%) was used. For the immobilization of active catalytic species, ammonium heptamolybdate tetrahydrate ($(NH_4)_6Mo_7O_{24}\cdot 4H_2O$, ≥99%) was employed as the metallic precursor. Dibenzothiophene (DBT) served as the representative refractory sulfur substrate for evaluating ODS performance. The DBT was dissolved in *n*-octane as the model fuel, and formic acid (HCOOH, 98 wt%) was used as a reaction modifier; DBT, *n*-octane, and HCOOH were sourced from Merck. All chemicals were of analytical grade and utilized as received without further purification. Distilled water was employed for all aqueous solution preparations and washing procedures (Fig. 1).

2.1.2. Preparation of PSBC. Initially, raw PS were cleaned by several washing cycles with distilled water to remove residual organic matter and surface contaminants. The cleaned biomass was then dried in an oven at 120 °C for 12 h, then mechanically ground, and the powder was passed through a 50-mesh stainless-steel screen to obtain a uniform particle size distribution. Before heating, nitrogen gas was flushed through the tubular furnace for enough time to completely replace residual air in the reactor column and to create an inert atmosphere. Pyrolysis was performed under a continuous nitrogen flow (5 mL min^{-1}). The temperature was ramped up at a controlled

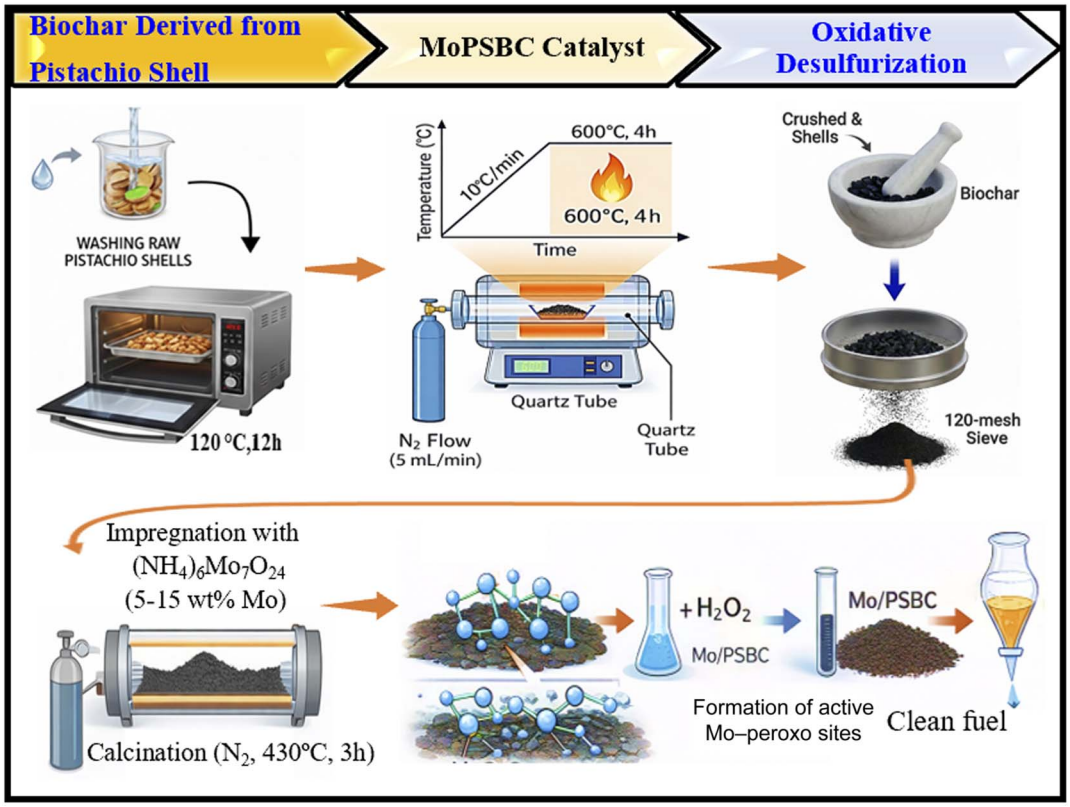

Fig. 1 Schematic of the MoO_2/pistachio shell biochar (MoPSBC) production *via* impregnation and carbothermal reduction.

heating rate of 10 °C min^{-1} to 600 °C and held at this temperature for 4 h to ensure complete carbonization and to promote pore development. After the thermal process, the furnace was allowed to cool naturally to room temperature under nitrogen in order to avoid surface oxidation of the newly prepared biochar. The resulting pistachio-shell-derived biochar (PSBC) was ground to a fine powder and passed through a 120-mesh sieve to give a uniform powder that was suitable for metal impregnation and catalytic applications.

In order to increase the surface area and introduce oxygen-containing functional groups, which would facilitate metal dispersion, the biochar was acid-activated. The material was added to 0.1 N nitric acid (HNO_3), at a solid-to-liquid ratio of 1 : 10 (w/v), and stirred for 24 h at room temperature. This treatment dissolves the remaining mineral impurities and generates surface functionalities, such as OH and COOH groups, which are sites for metal species. The activated biochar was filtered and extensively washed with distilled water until the filtrate became neutral according to a calibrated pH meter. Finally, the sample was dried at 110 °C for 24 h and kept in a desiccator before metal impregnation.

2.1.3. Fabrication of Mo/PSBC catalysts *via* wet impregnation. The MoO_2-loaded catalysts were produced *via* the wet impregnation method. To obtain biochar with a theoretical molybdenum loading of 5, 10, and 15 wt%, respectively, aqueous solutions of ammonium heptamolybdate tetrahydrate ($(NH_4)_6Mo_7O_{24}\cdot 4H_2O$) were prepared with their concentrations very precisely calibrated. The HNO_3-functionalized biochar (PSBC) was gradually added to the precursor solutions and the mixture was magnetically stirred vigorously for 24 h at room temperature; this extended contact time was employed to promote strong anchoring of the polyoxometalate ions on the surface functional groups that are rich in oxygen and to allow the ions to diffuse deeply into the hierarchical pore structure. After the impregnation period, the mixture was filtered, and the resulting product was dried in an oven at 110 °C for 12 h to remove residual moisture and to fix the metal layer derived from the precursor on the carbonaceous support.

The dried impregnated samples were thermally treated in a horizontal tubular furnace at a very precise temperature to allow the molybdenum precursor to decompose and form the active catalytic sites. In order to allow the formation of MoO_2 and to avoid bulk MoO_3, the process was carried out under a strictly inert nitrogen atmosphere with a continuous flow of 5 mL min^{-1}. The temperature of the furnace was increased at a rate of 5 °C min^{-1} until it reached a final temperature of 450 °C and was kept for 3 h at that temperature. This temperature window was intentionally used to benefit from the reducing environment of the biochar matrix, which results in the partial reduction of Mo^{6+} centers. After being calcined, the catalysts were cooled to room temperature under a protective nitrogen flow so that the surface was not re-oxidized. The final products, which are referred to as *x*MoPSBC (x = 5, 10 or 15 wt%), were

taken from the reaction and kept in airtight glass containers for further ODS tests.

2.2. Instrumentation

The crystalline structure of the catalysts was analyzed using X-ray diffraction (XRD) with Cu Kα radiation ($\lambda = 1.5406$ Å) over a 2θ range of 9.59–79.99°. Functional groups were identified by Fourier-transform infrared (FTIR) spectroscopy. Scanning electron microscopy coupled with energy-dispersive X-ray spectroscopy (SEM-EDX) was used to determine surface morphology and elemental composition, and the thermal properties were determined using differential scanning calorimetry (DSC) analysis. Energy-dispersive X-ray fluorescence (ED-XRF) analysis was used to determine the level of sulfur in the fuel samples, and UV-visible spectroscopy was used as a complementary method to identify the variation in aromatic sulfur compounds during oxidation. All thermal processes were carried out in a tubular furnace in a continuous nitrogen atmosphere.

2.3. Systematic optimization and catalytic performance evaluation

The catalytic efficiency of *x*MoPSBC was tested by using a high-sulfur model fuel (10 000 ppm DBT and 1737 ppm S) as well as refinery-grade diesel (1715 ppm S). The research was designed in two stages: in the first stage, a promoter-free univariate optimization of temperature (30–70 °C), catalyst dosage (0.02–0.1 g), reaction time (10–60 min), and H_2O_2/S-organic compounds molar ratio (2, 4, 6, or 8) was done to determine the inherent activity of the MoO_2 sites, and to establish the ideal dose of oxidants that would be needed for effective desulfurization.

Then, formic acid (HCOOH) was added in the second phase to assess the synergistic effect on the oxidation kinetics under the optimum conditions. To ensure analytical rigor, sulfur determination followed a dual-instrumental approach. Energy-dispersive X-ray fluorescence (ED-XRF) analysis was employed for the direct measurement of total sulfur levels, while UV-vis spectroscopy provided secondary confirmation by monitoring the characteristic electronic transitions of the aromatic organosulfur rings. Based on the instrumental calibration and analytical sensitivity, the experimental uncertainty was determined to be ±1.0%. Consequently, all conversion values are reported to one decimal place to reflect this precision. The total desulfurization efficiency (η%) was determined from the concentration change as follows:

$$(\eta\%) = \frac{C_o - C_t}{C_o} \times 100,$$

where C_o and C_t denote the sulfur concentrations (ppm) in the original sample and at time t, respectively.

3 Results and discussion

The development of high-performance heterogeneous catalysts for ODS depends largely on the rational engineering of porous supports and the accurate dispersion of active metal phases. In this study, the structure–activity relationships of the PSBC-supported catalysts were systematically elucidated through the correlation of state-of-the-art microscopic imaging with spectroscopic and diffraction data. This analysis explains the mechanisms that enable the rapid transformation of refractory organosulfur compounds, even at high concentrations (10 000 ppm) representative of heavy industrial feedstocks.

3.1. Morphological evolution and surface engineering (FESEM)

As demonstrated by FESEM analysis, PSBC exhibits a dense, relatively non-porous topography with longitudinal vascular structures (Fig. 2a). The compact structure is confirmed by EDX analysis (Fig. 2d), showing a carbon-rich matrix (93.52 wt%) with a very low oxygen content (6.44 wt%) and trace mineral residuals.

The HNO_3 activation operates through two simultaneous and complementary mechanisms. First, HNO_3 acts as a potent chemical de-ashing and etching agent, removing volatile organic compounds that obstruct microporous channels and dissolving unstable volatile components (Fig. 2b), thereby significantly increasing the accessible surface area for organosulfur molecule diffusion. This structural enhancement is evidenced by the increase in carbon purity to 93.99 wt% as confirmed by elemental analysis (Fig. 2e). Second, the oxidizing nature of HNO_3 chemically transforms the biochar surface by generating oxygenated functional groups, specifically carboxyl (–COOH), carbonyl (–C=O), and hydroxyl (–OH) groups.[47] This surface transformation transitions the biochar from a catalytically inert state to a high-energy hydrophilic template that is highly suitable for metal coordination, thereby facilitating uniform dispersion and strong anchoring of Mo active species on the support surface.

Following molybdenum oxide impregnation and calcination, the MoPSBC catalyst exhibits a significant topographical shift. The rugose carbon facets become decorated with well-defined polyhedral crystallites and sub-micron clusters (Fig. 2c). A quantitative EDX analysis (Fig. 2f) verified the Mo surface loading at 5.03 wt%. Furthermore, the elevated oxygen content (6.33 wt%) is a strong indication of the formation of catalytic MoO_2 species.

The elemental mapping (Fig. 2g–j) offers incontestable evidence of spatial homogeneity, as it shows that Mo was highly dispersed all over the hierarchical framework, instead of only being surface agglomerated (Fig. 2j). Consequently, the combination of hierarchical porosity and strong metal–support interactions give a well-defined structure–activity relationship: the etched macro channels serve as the high-velocity diffusion "highways" for dibenzothiophene (DBT) molecules, and, at the same time, the evenly distributed molybdenum oxide sites enable fast oxygen transfer through reactive peroxo molybdate intermediates. This hierarchical pore architecture is particularly advantageous for DBT, a bulky refractory organosulfur compound with significant steric hindrance, as the macroporous channels minimize external diffusion resistance while the mesopores provide a high density of accessible MoO_2 active

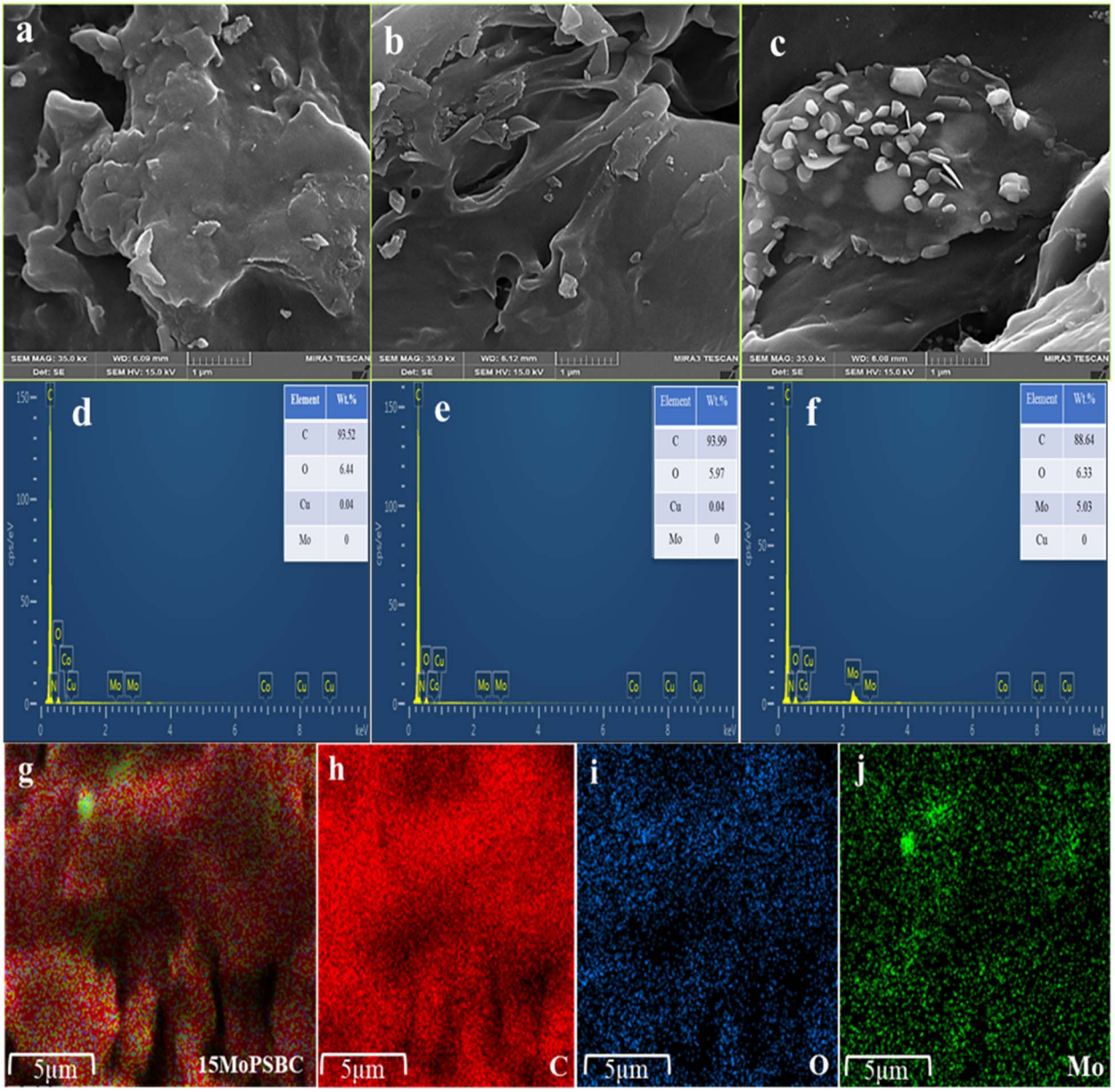

Fig. 2 Scanning electron microscopy (SEM) images of (a) PSBC, (b) activated PSBC and (c) MoPSBC. EDS analysis of (d) PSBC, (e) activated PSBC, and (f) MoPSBC. EDS elemental mapping images of (g) 15MoPSBC, (h) C, (i) O, and (j) Mo.

sites, collectively ensuring efficient molecular transport and oxidation. Hence, this meticulously designed structure is basically the major factor behind the catalyst's outstanding performance in deep industrial fuel purification.

The crystallographic transformation of MoO_2 species from the impregnated precursor to the stabilized catalyst phase was investigated using X-ray diffraction (XRD), as presented in Fig. 3. To evaluate the phase purity and the extent of the chemical reduction under distinct thermal environments, diffraction profiles were cross-referenced with orthorhombic α-MoO_3 (Molybdite, Ref. Code 96-101-1074) and monoclinic MoO_2 (Tugarinovite, Ref. Code 96-900-9091) standards.

The pristine biochar (Fig. 3a) exhibits a broad diffraction halo centered around $2\theta \approx 23°$, characteristic of the disordered, amorphous carbon matrix derived from PS pyrolysis. In contrast, the sample calcined under atmospheric conditions at 450 °C (Fig. 3e) unequivocally indexes to the orthorhombic α-MoO_3 crystal system (space group *Pnma*), representing molybdenum in the fully oxidized Mo^{6+} state. Well-defined reflections appear at $2\theta = 12.93°$, 23.54°, 25.89°, 27.52°, 33.96°, and 39.16°. Notably, the peaks at 12.93°, 25.89°, and 39.16° form an (*h*00) harmonic series corresponding to the (200), (400), and (600) planes, respectively. This sequence serves as a diagnostic fingerprint of the layered α-MoO_3 structure, confirming an ordered stacking of MoO_6 octahedra along the *a*-axis.

A profound structural metamorphosis is observed for the samples calcined at 450 °C under an inert nitrogen atmosphere (Fig. 3b–d). The complete disappearance of the characteristic α-

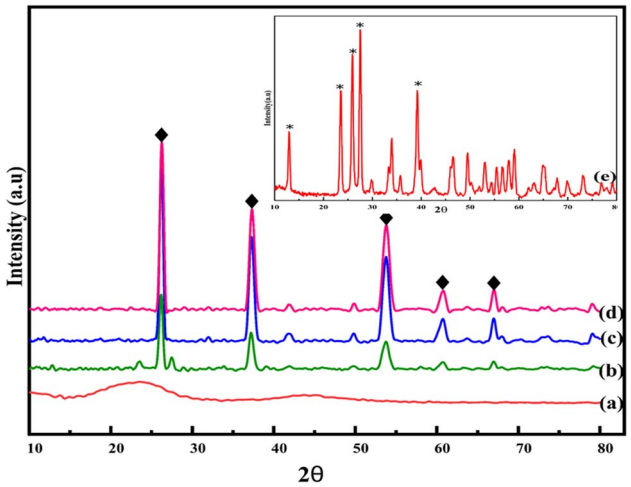

Fig. 3 X-ray diffraction (XRD) patterns of the (a) acid-activated PSBC, (b) 5MoPSBC, (c) 10MoPSBC, and (d) 15MoPSBC catalysts, with all traces showing the characteristic diffraction peaks of monoclinic MoO_2 (marked with ◆). (e) XRD pattern of the 10MoPSBC sample identifying the layered orthorhombic α-MoO_3 phase (marked with *).

MoO_3 reflection at 12.93° signals the collapse of the layered orthorhombic lattice and the completion of a carbothermal reduction process. The resulting diffractograms for 5MoPSBC (Fig. 3b), 10MoPSBC (Fig. 3c), and 15MoPSBC (Fig. 3d) are indexed to the monoclinic MoO_2 phase (space group $P2_1/c$) with a distorted rutile-type lattice. The primary evidence for the $Mo^{6+} \rightarrow Mo^{4+}$ transition is the emergence of the predominant reflection at $2\theta \approx 26.10°$, assigned to the $(\bar{1}11)$ plane. Successful reduction is further corroborated by secondary reflections at 37.33° (111), 53.95° ($\bar{2}22$/022), 61.10° ($\bar{1}13$), and 67.07° (311).

The sharp intensity and narrow full width at half maximum (FWHM ≈ 0.443°) observed in the 15MoPSBC sample imply that the biochar matrix facilitated the growth of highly crystalline MoO_2 nanoparticles. This phase stabilization is mediated by the carbonaceous host, which acts as a solid-state reducing environment wherein the lattice oxygen of molybdenum species reacts with the biochar carbon. The persistence of the amorphous carbon halo confirms that the biochar acts as a robust support, anchoring MoO_2 particles and preventing sintering, despite high metal loading. The anchoring mechanism is attributed to strong coordinative interactions between the oxygen-containing functional groups (–COOH, –OH, and –C=O) present on the amorphous carbon surface and the Mo species, which immobilize MoO_2 crystallites and act as physical barriers against particle migration. However, at the 15 wt% loading level, incipient aggregation is observed as the concentration of Mo species exceeds the monolayer dispersion capacity of the PSBC surface. When the functional anchoring sites are saturated, other molybdenum species react selectively with each other, resulting in multi-layer deposition and partial clustering. The XRD results support this behavior by revealing the appearance of crystalline MoO_2 peaks, which means that larger particles based on Mo were formed. As a result, the effective metal–support interfacial contact area of this aggregation is less than that of the lower loading samples. This complete conversion is critical for catalytic efficacy; the metallic-like conductivity of the monoclinic MoO_2 phase allows superior charge transfer and, thus, the formation of reactive peroxo molybdate intermediates is more pronounced than with the MoO_3 semiconducting precursor, driving deep ODS of high-concentration feedstocks.

Both the crystallographic and morphological results have indisputably demonstrated the successful incorporation of monoclinic MoO_2, which is well-dispersed in the carbonaceous matrix. To investigate the surface chemistry, which is responsible for this metal–support synergism, the catalyst series was systematically analyzed by Fourier-transform infrared (FTIR) spectroscopy.

The structural evolution and surface functional groups of raw PS, PSBC, and *x*MoPSBC were investigated using FTIR spectroscopy, as shown in Fig. 4. Compared with raw PS, the spectra of PSBC and MoPSBC samples exhibit significant attenuation or disappearance of several absorption bands, which indicates that oxygen-containing and aliphatic functional groups were thermally decomposed during pyrolysis. The broad absorption band at 3250–3500 cm^{-1} in the PS corresponds to OH stretching vibrations of hydroxyl groups and hydrogen-bonded species originating from cellulose, hemicellulose, and lignin. After pyrolysis, this band decreases markedly, confirming dehydration and structural decomposition of biomass components. A slight weakening and a red shift after the addition of molybdenum suggest a possible interaction between surface hydroxyl groups and the molybdenum species.[48,49] The strong bands at 2860–2930 cm^{-1}, assigned to symmetric and asymmetric stretching of aliphatic $–CH_2/–CH_3$ groups, along with the bending vibration at approximately 1379 cm^{-1}, are prominent in PS but substantially reduced in PSBC. This diminution confirms the breakdown of aliphatic chains and progressive aromatization during carbonization. The further decrease in MoPSBC samples reflects continued structural condensation and surface modification.[50,51]

The band located near 1738 cm^{-1}, corresponding to the C=O stretching vibration of carbonyl and carboxylic functional

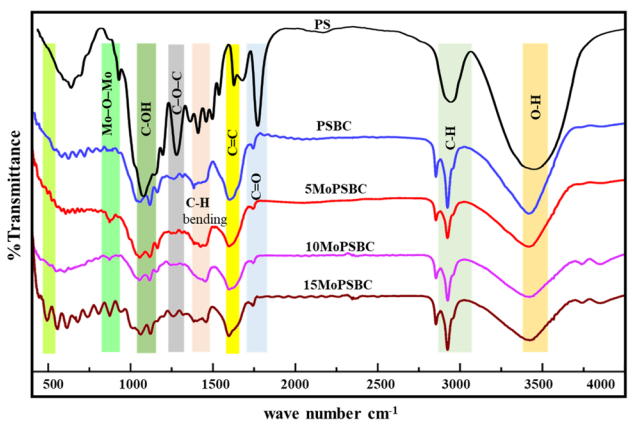

Fig. 4 FTIR spectral analysis of the surface functional groups of the PS, PSBC, and *x*MoPSBC (*x* = 5, 10 and 15) catalysts.

groups, diminishes after pyrolysis due to decarboxylation reactions. In Mo-loaded biochar, variations in the intensity and position of this band suggest coordination between carbonyl oxygen atoms and Mo species. The formation of condensed aromatic structures is supported by a strong peak at around 1580–1610 cm^{-1}, attributed to aromatic C=C stretching vibrations, which becomes more intense in PSBC and *x*MoPSBC samples.[52,53] The band at 1244 cm^{-1} is attributed to C–O–C stretching within the cellulose backbone.[54] In addition, absorption bands between 1030–1150 cm^{-1}, attributed to C–O stretching modes of alcohols and phenols, diminish upon pyrolysis, consistent with the loss of polysaccharide-derived oxygenated functionalities.[45,55] In the case of MoPSBC samples, especially 15MoPSBC, a distinct band at 873 cm^{-1} is observed, attributed to Mo–O–Mo stretching vibrations. Additionally, the band at approximately 485 cm^{-1} corresponds to Mo–O stretching, confirming the presence of molybdenum oxide species anchored on the biochar surface.[56] Overall, the FTIR results demonstrate progressive transformation from oxygen-rich lignocellulosic biomass to an aromatic carbon framework, followed by successful incorporation of MoO_2 species without significant disruption of the carbon backbone. These coordinative interactions between surface functional groups and Mo species, evidenced by the red shift and attenuation of –OH and C=O bands, further corroborate the anchoring mechanism responsible for preventing MoO_2 sintering at high metal loadings. To complement the spectroscopic evidence, DSC analysis was conducted to probe the thermal stability and metal–support interaction strength across the MoPSBC catalyst series.

The thermal stability and phase transformation characteristics of the original PS, PSBC, and the MoPSBC catalyst series were systematically elucidated by differential scanning calorimetry (DSC) over the temperature range of 25–560 °C, as shown in Fig. 5. The raw PS displays a thermally complex exothermic profile, reflecting its heterogeneous lignocellulosic composition. A broad exothermic event at 365 °C is ascribed to the overlapping thermal degradation of hemicellulose and the amorphous cellulose fraction components, whereas two sharp and well-resolved exothermic peaks at 522 °C and 539 °C correspond to the successive oxidative degradation of structurally distinct lignin domains, a multi-stage combustion signature consistent with the hierarchical thermal recalcitrance of lignocellulosic biomass widely reported in the literature.

Following pyrolytic conversion, the PSBC profile undergoes a fundamental transformation, wherein the low-temperature cellulosic decomposition event at 365 °C is entirely suppressed, and the double lignin peaks consolidate into a single, broad exothermic peak at 506 °C. This dramatic simplification of the thermal profile provides compelling calorimetric evidence for the successful carbonization of thermally labile organic fractions during pyrolysis, signifying the transition toward a structurally more homogeneous, thermally resilient, and graphically integrated carbonaceous framework. The upward shift of the residual exothermic event further reflects the greater thermal recalcitrance of the turbostratic carbon matrix formed during high-temperature pyrolysis.

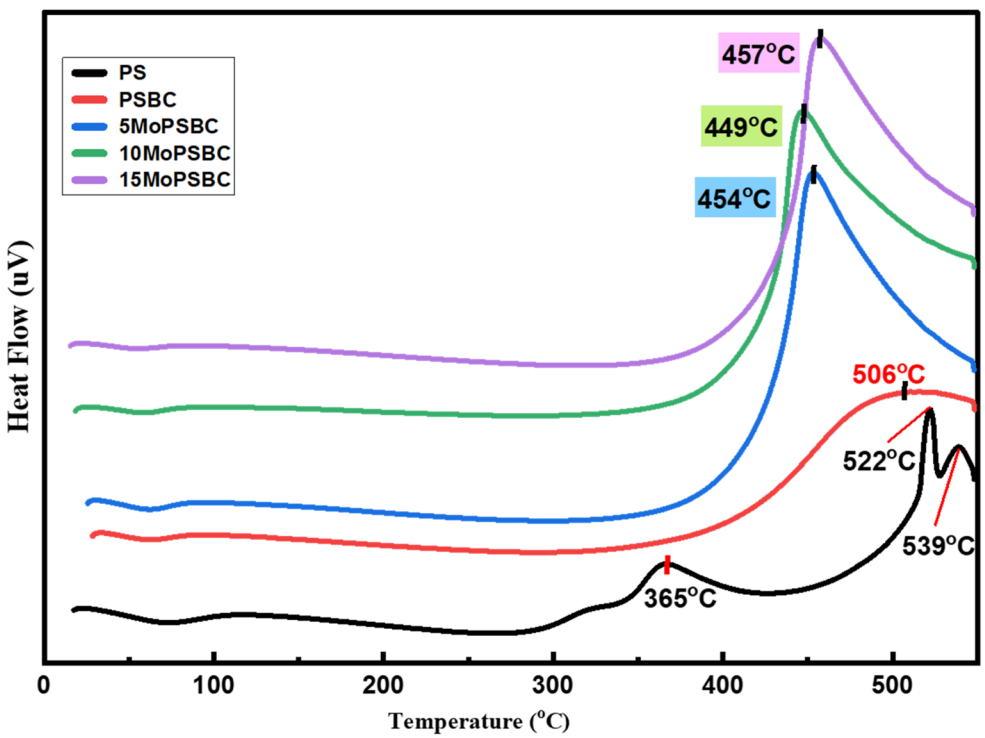

Fig. 5 DSC profiles of the PS, PSBC, and MoPSBC catalysts (5, 10, and 15 wt% Mo), revealing their thermal stability and metal–support interaction effects.

Introducing MoO_2 on the surface of biochar induces a pronounced and mechanistically significant downward shift in the temperature of the main exothermic peak from 506 °C, for bare PSBC, to 454 °C, 449 °C, and 457 °C for 5MoPSBC, 10MoPSBC, and 15MoPSBC, respectively. This systematic depression in peak temperature is attributed to two complementary phenomena: the first is the well-established catalytic gasification effect of redox-active transition-metal oxides, where surface MoO_2 species lower the activation energy for carbon–oxygen bond-formation and thus enable faster oxidative decomposition of the biochar matrix. The second is the possible role of the crystallization energy of the monoclinic MoO_2 phase, which may superimpose an exothermic thermal signature at lower temperatures upon molybdenum incorporation. The substantially sharper and more intense exothermic peaks of all MoPSBC samples compared to that of the bare PSBC further confirm intimate interfacial contact between MoO_2 nanoparticles and the graphitic carbon surface, thus indicating strong metal–support interactions that are essential for effective H_2O_2 activation in ODS.

Particularly noteworthy is the non-monotonic relationship between Mo loading and peak temperature: the minimum exothermic temperature is observed for 10MoPSBC (449 °C), while 15MoPSBC exhibits a marginal reversal to 457 °C. This behavior is consistent with an optimal dispersion of MoO_2 nanoparticles at 10 wt% loading, maximizing metal–support contact area and interaction energy. At 15 wt% loading, incipient aggregation or partial clustering of Mo species decreases the contact area between the metal and the support materials, thus diminishing the gasification and crystallization processes and leading to a temperature rise. Critically, this observation is fully corroborated by the catalytic performance data, where the ODS activity difference between 10MoPSBC and 15MoPSBC was found to be marginal, confirming that 10 wt% represents the optimal balance between active site density and dispersion efficiency.

Equally significant is the flat, featureless baseline observed for all MoPSBC catalysts between 25 °C and approximately 380 °C, spanning the entire operational temperature window of the ODS process (40 °C to 70 °C) by a substantial margin. This thermal inertness confirms the complete absence of endothermic or exothermic phase transitions, structural rearrangements, or decomposition events under the reaction conditions. These findings provide strong calorimetric evidence for the operational stability and structural integrity of the MoPSBC catalyst platform. Collectively, the DSC analysis not only validates the successful synthesis of thermally robust molybdenum oxide functionalized biochar catalysts but also reveals essential structure–property relationships between Mo dispersion, metal–support interaction strength, and catalytic performance, which are fully consistent with the observed ODS activity trends.

3.2. Assessment of oxidative desulfurization efficiency

3.2.1. Effect of reaction conditions. The influence of catalyst dosage on ODS efficiency was systematically evaluated to

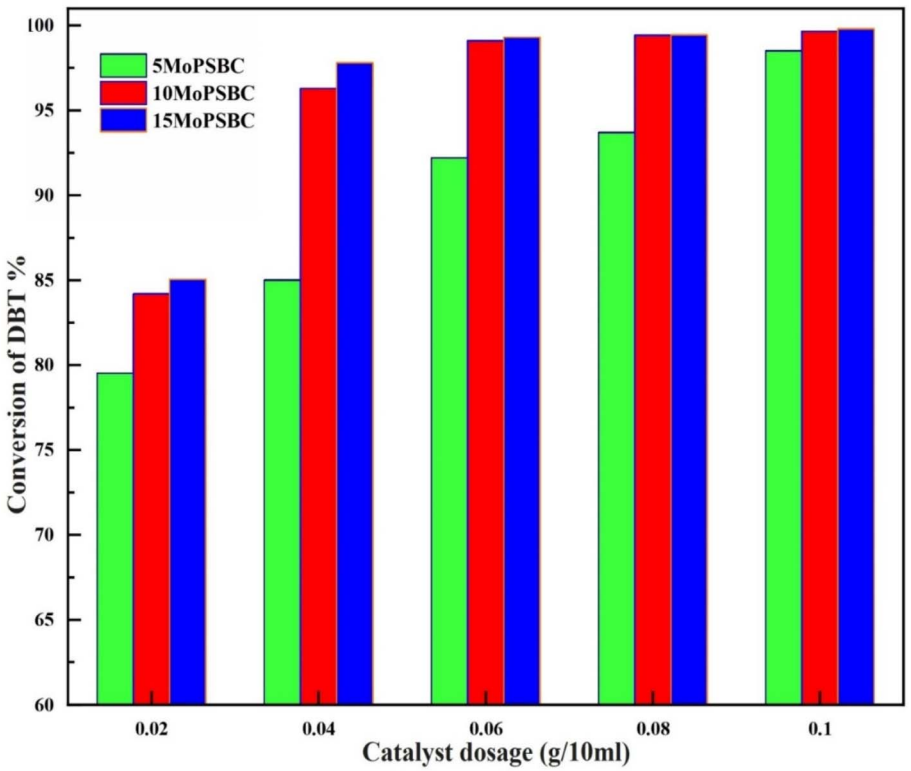

Fig. 6 Effect of the catalyst dosage (g) on the conversion of DBT (%) using 10 000 ppm of DBT model fuel (10 mL, H_2O_2/S molar ratio = 6, 70 °C, and 60 min). Note: for this and all subsequent figures, the instrumental error is ±1.0%.

identify the threshold required for near-complete sulfur removal from a 10 000 ppm DBT model fuel. As shown in the catalytic performance profiles (Fig. 6), DBT conversion increased sharply and non-linearly as the dosage of 15MoPSBC was increased from 0.02 g to 0.10 g. An optimal dosage of 0.06 g per 10 mL reaction system enabled a conversion exceeding 99.3% within 60 min under constant oxidant conditions. The observed enhancement can be primarily attributed to increased density of accessible MoO_2 active sites and surface hydroxyl functionalities acting as Lewis acidic centers. These sites enable H_2O_2 adsorption and activation *in situ* to produce reactive peroxo-molybdenum (Mo–O–O*) intermediates that oxidize DBT. The gradual leveling off in catalytic activity beyond 0.06 g indicates that the system transitions from active-site limitations to mass-transfer and oxidant limitations, which prevent further surface area increases from improving conversion. At this stage, the intrinsic catalytic capacity surpasses the rate of reactant diffusion and oxidant availability, resulting in a performance plateau.

The thermal activation behavior of the MoPSBC catalyst series was systematically investigated over the temperature range of 30–70 °C (Fig. 7). As expected, a clear temperature-dependent increase in desulfurization activity was observed for all formulations. At 30 °C, DBT conversion values were 66.7%, 70.2%, and 71.3% for 5MoPSBC, 10MoPSBC, and 15MoPSBC, respectively (with an estimated experimental error of ±1.0%). This loading-dependent activity ordering was maintained as temperatures increased. The most pronounced rate acceleration occurred between 50 °C and 70 °C, where 10MoPSBC and 15MoPSBC achieved near complete DBT conversion (>99.0%). The convergence of catalyst performance at higher temperatures suggests that the system approaches oxidant-limited conditions, with further conversion improvements becoming independent of the MoO_2 loading.

The exceptional efficiency achieved at 70 °C in the complete absence of acid co-promoters, such as carboxylic acid, to generate per acids for effective organosulfur oxidation represents a significant practical advantage over conventional ODS systems. In contrast, the MoPSBC platform operates as an intrinsically self-activating system, wherein the metallic-like conductivity of the monoclinic MoO_2 phase, acting synergistically with oxygen-containing surface functionalities of the biochar support, facilitates direct H_2O_2 activation and lowers the apparent activation barrier for oxidation of the refractory DBT molecule. The progressive enhancement in conversion with temperature is therefore explained by accelerated Mo^{4+}/Mo^{6+} redox cycling and increased generation of electrophilic oxoperoxo-molybdenum intermediates, all of which direct the reaction to near completion within mild, yet industrially relevant conditions.

The molar ratio of oxidant to sulfur (O/S) is a fundamental parameter in the ODS process, as it governs both stoichiometric efficiency and process economics. In theory, the complete oxidation of one mole of dibenzothiophene (DBT) to its corresponding sulfone ($DBTO_2$) requires two molar equivalents of H_2O_2. Practically, the oxidant level must overcome non-

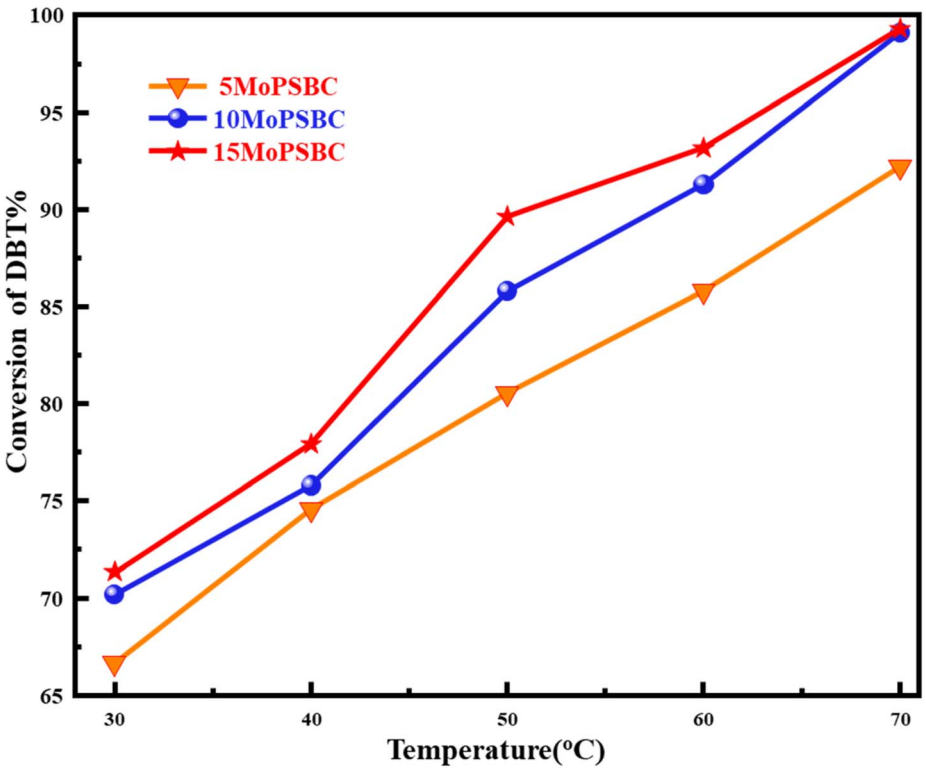

Fig. 7 Effect of the reaction temperature on the conversion of DBT (%) over the *x*MoPSBC catalysts (conditions: 10 mL of model fuel, 10 000 ppm of DBT, catalyst dosage = 0.06 g, H_2O_2/S = 6, and reaction time = 60 min).

productive thermal degradation of H_2O_2 as well as interfacial mass-transfer limitations between the aqueous phase and the oil phase.

As illustrated in Fig. 8, the desulfurization efficiency of both 10MoPSBC and 15MoPSBC was evaluated at H_2O_2/S ratios ranging from 2 to 8. It was found that at the stoichiometric proportion of H_2O_2/S = 2, 10MoPSBC and 15MoPSBC reached baseline conversions of 93.0% and 95.3%, respectively, indicating that the higher the Mo loading, the greater the overall density of active sites for peroxide activation, even under oxidant-deficient conditions. The improvement was more pronounced with the subsequent increase in the H_2O_2/S ratio from 2 to 6, with DBT conversion percentages of 99.1% and 99.3% for 10MoPSBC and 15MoPSBC, respectively. This tendency indicates a shift from the oxidant-limited regime to stoichiometric sufficiency when molybdenum oxide active sites become practically occupied by reactive oxygen atoms. Additional increases in the ratio to O/S = 8 yielded only a marginal increase (99.3% and 99.5%); therefore, the reaction seems to approach a kinetic plateau wherein further oxidant addition provides no discernible benefit. Considering this, H_2O_2/S = 6 is identified as the optimal condition, balancing near-complete DBT conversion with minimal reagent consumption and oxidant waste.

The temporal evolution of DBT conversion over the MoPSBC catalyst series was systematically investigated at 70 °C under optimized conditions (H_2O_2/S = 6 and catalyst dosage = 0.06 g), with results presented in Fig. 9a and b, for the unpromoted and formic acid-promoted systems, respectively. In the absence of any co-promoter (Fig. 9a), all the catalyst formulations showed a monotonically increasing conversion-time profile during the entire 60 minutes of reaction, thus revealing that the oxygen-dispersed sulfide (ODS) process is kinetically determined by the surface density of available Mo^{4+}/Mo^{6+} redox centers rather than by oxidant availability or interfacial diffusion constraints. This loading-dependent activity hierarchy was also prominently observed at the earliest measured time point: conversions of 80.1%, 81.7%, and 87.2% were recorded for 5MoPSBC, 10MoPSBC and 15MoPSBC, respectively, at 10 min, and progressively increased throughout the reaction period to final conversions of 92.2%, 99.1%, and 99.3%, respectively, at 60 min. Those percentage gains of 6.9-percentage points between 5MoPSBC and 10MoPSBC, compared with 0.2-percentage points between 10MoPSBC and 15MoPSBC, at 60 min are strong kinetic indicators of an optimal Mo loading of about 10 wt%, above which incipient aggregation suppresses the active-site accessibility without corresponding proportional improvement in catalytic performance, as also independently supported by differential scanning calorimetry (DSC) thermal analysis.

The introduction of formic acid as an *in situ* oxidant precursor (Fig. 9b) generated a transformative and mechanistically distinctive kinetic acceleration that fundamentally altered the conversion-time landscape across all catalyst

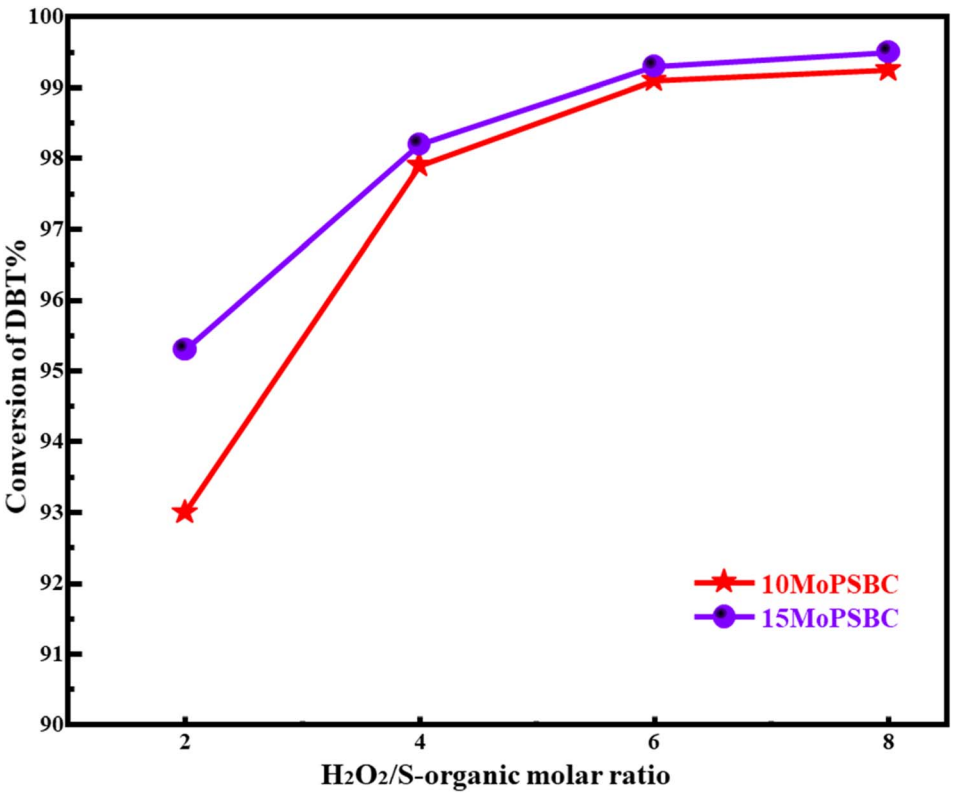

Fig. 8 Effect of the H_2O_2/S-organic molar ratio on the DBT conversion efficiency over the 10MoPSBC and 15MoPSBC catalysts (catalyst dosage = 0.06 g, T = 70 °C, t = 60 min, 10 mL of model fuel, and 10 000 ppm of DBT).

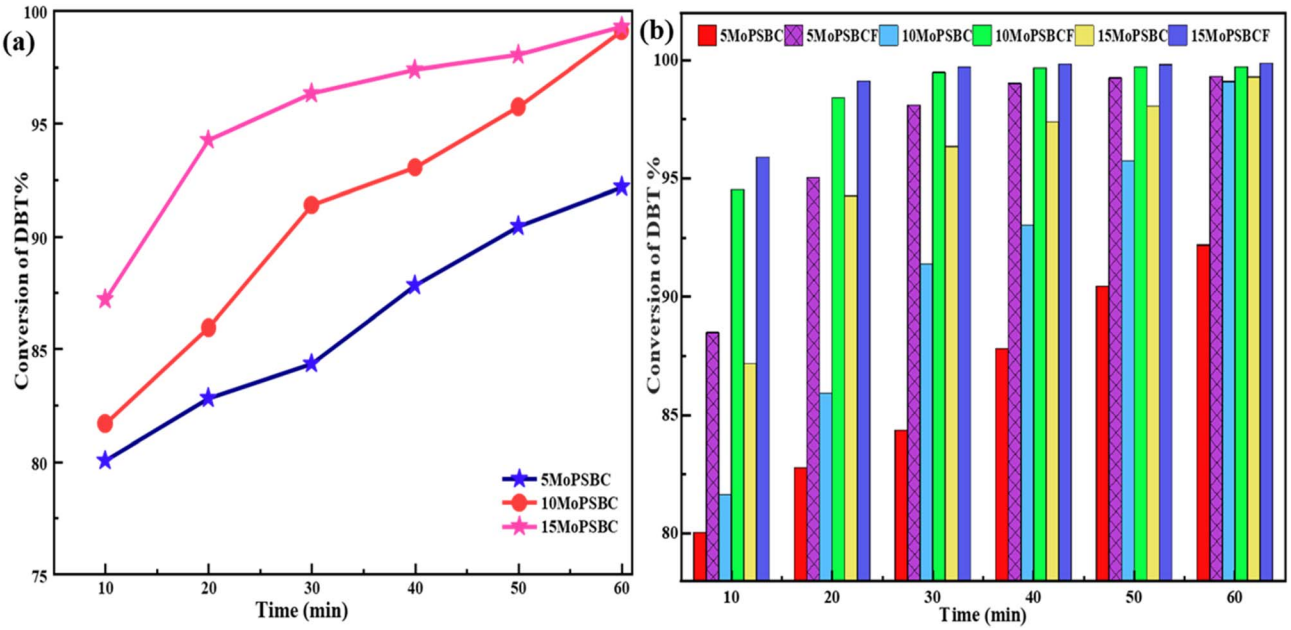

Fig. 9 DBT conversion as a function of the reaction time over (a) unpromoted MoPSBC and (b) formic acid-promoted MoPSBCF catalysts (5–15 wt% Mo) at 70 °C under the optimized conditions (H_2O_2/S-organic molar ratio = 6 and catalyst dosage = 0.06 g).

formulations. The promoted catalysts also performed better at the earliest normalized time of 10 min of analysis, with conversions of 88.5%, 94.5%, and 95.9% for 5MoPSBCF, 10MoPSBCF, and 15MoPSBCF, respectively. These conversions are better by large margins than their unpromoted counterparts and demonstrate a significant time compression of the effective reaction timescale by the promoted catalysts. The approach to near-complete conversion was remarkably rapid. After 30 min, 10MoPSBCF and 15MoPSBCF reached 99.5% and 99.7% conversion, respectively, while 15MoPSBCF attained 99.9%. After 60 min, all promoted formulations achieved conversions of 99.3% or higher.

This strong promotional effect is attributed to the *in situ* formation of performic acid (HCOOOH) *via* a well-established acid-catalyzed equilibrium reaction between formic acid and H_2O_2 as follows:

$$HCOOH + H_2O_2 \rightleftharpoons HCOOOH + H_2O.$$

This intermediate was not measured directly in the present study, but is well known in the literature on ODS. Performic acid is a powerful liquid-phase electrophilic oxygen carrier, and, at the same time, its presence enables stabilization of electrophilic peroxo-molybdenum complexes on the catalyst surface.[57–60] This forms a synergistic dual pathway in which the homogeneous oxidant will circumvent the steric hindrance of the large DBT molecules, and the heterogeneous MoO_2 sites will provide a high density of active sites. This synergy is effective in breaking down kinetic barriers, resulting in the time-compression effect and faster rates of desulfurization.

The most economically relevant finding of this comparative study is that the 60-min conversion of the formic acid-promoted 5MoPSBCF (99.3%) exceeds the same time-point conversion of the unpromoted 15MoPSBC (99.3%) by far, even though 5MoPSBCF has significantly lower concentrations of molybdenum oxide. This clearly shows that acid co-activation decouples catalytic activity from metal loading, thereby providing an economically efficient, rational, and scalable approach to ultra-deep desulphurization under mild, industrially relevant conditions in which strategic acid promotion allows the same or even better performance at a lower catalyst cost.

3.2.2. Investigation of real diesel fuel. Following the optimization studies, which established 70 °C, 60 min, H_2O_2/S = 6, and a catalyst dosage of 0.06 g as the optimal reaction conditions, the practical applicability of the MoPSBC catalytic system was evaluated using a real gas oil feedstock containing 1715 ppm sulfur. This evaluation was conducted to show whether the performance patterns noted in the model DBT system were viable in a complex hydrocarbon matrix. Fig. 10 demonstrates that there is a systematic increase in the efficiency of desulfurization along the series of experiments. System A (solvent extraction) was able to extract only 15.4% of the sulfur, which proves that physical partitioning cannot be used to deeply desulfurize the system under the optimized conditions. The small decreases in sulfur recorded with H_2O_2 (32.3%) and formic acid (37.4%) alone further confirm that neither of the compounds is sufficiently oxidative to activate recalcitrant sulfur compounds found in real fuel.

Upon introduction of the MoPSBC catalyst under the same optimized parameters, significant performance improvement was achieved. The 5MoPSBC and 10MoPSBC systems were able to achieve 66.8% and 76.6% sulfur removal, respectively, which means that the Mo active sites are free even when aromatics and other matrix elements in the actual feed are competing with the

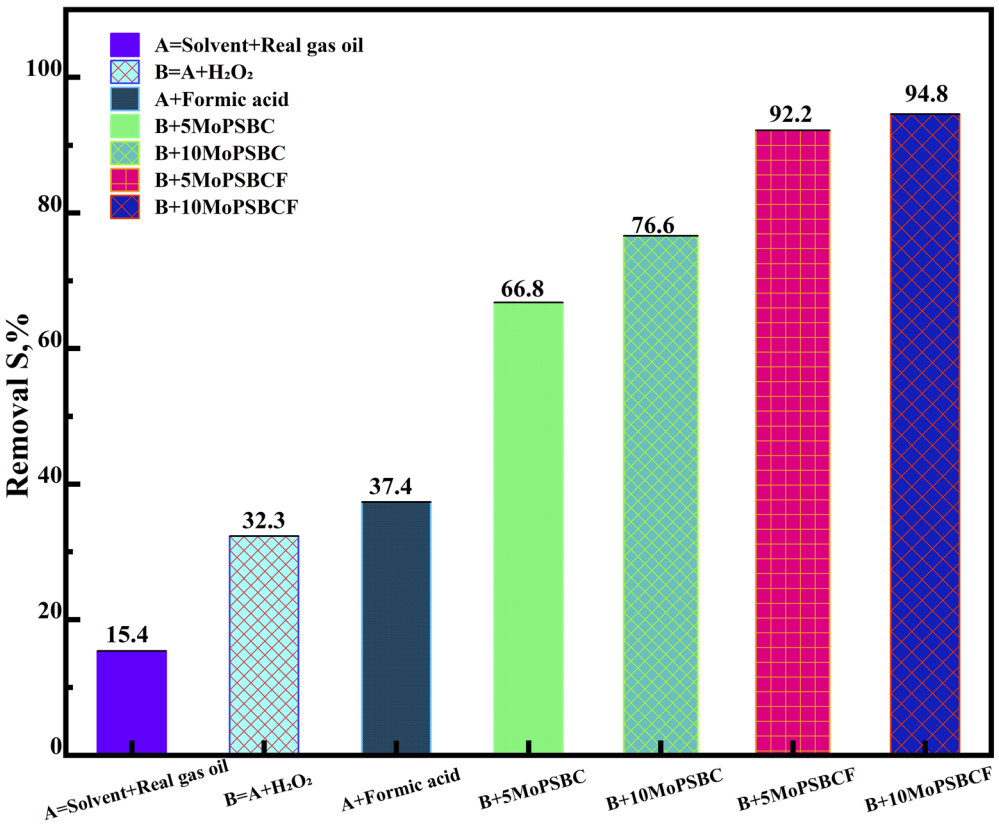

Fig. 10 Evaluation of the performance of the MoPSBC catalytic system in a real gas oil matrix (conditions: 10 mL of gas oil, initial $S = 1715$ ppm, 0.06 g of catalyst, 60 min, H_2O_2/S-organic molar ratio = 6, and 70 °C).

system. These results confirm that the catalytic activity identified during optimization is retained in a more demanding reaction environment.

This sustained performance in a complex feedstock is attributed to the preferential electrophilic attack of the stabilized peroxo-molybdenum intermediates. In a real fuel matrix, aromatic hydrocarbons compete for active sites; however, the MoO_2-based active centers exhibit a high degree of chemoselectivity toward the sulfur atom in DBT due to its superior nucleophilicity compared to typical aromatic rings. Additionally, the hierarchical porosity of the PSBC framework minimizes the inhibitory effects of the matrix by providing large macrochannels that prioritize the diffusion of bulky organosulfur compounds, thereby ensuring that the molybdenum active sites remain functionally free and accessible even under competitive industrial conditions.

Notably, the formic acid-promoted 10MoPSBCF reached a remarkable 94.8% removal, reducing the sulfur level to approximately 89 ppm. This performance is highly significant; it demonstrates that the synergistic *in situ* generation of performic acid works in tandem with peroxo molybdenum intermediates to lower the kinetic barriers for sterically hindered species, such as dibenzothiophene, which typically resist standard HDS.

Notably, the fact that the promoted 5MoPSBCF (92.2%) outperformed the unmodified 10MoPSBC (76.6%) at half the metal loading provides a compelling argument for the economic and environmental viability of this system. By maximizing active-site utilization through acid co-activation, the MoPSBCF platform offers a scalable and robust pathway for achieving near-ULSD standards in complex refinery streams, even under moderate operating conditions.

3.2.3. Kinetic study. The conversion-time profiles that were obtained under the above conditions were later subjected to quantitative kinetic analysis to determine the inherent reaction rates and elucidate the mechanistic role of MoO_2 loading and formic acid promotion. As shown in Fig. 11 and tabulated in Table 1, the linear fit of $-\ln(C_t/C_0)$ against the reaction time for all catalyst formulations confirmed that the oxidation of DBT over the MoPSBC series follows pseudo-first-order reaction kinetics with respect to DBT concentration. This is in line with the fact that an excess amount of H_2O_2 was present in the reaction.

Without formic acid, the rate constant changes from $k = 0.01918$ min^{-1} for 5MoPSBC to $k = 0.05392$ min^{-1} for 10MoPSBC, a 2.8-fold increase; thus, it is confirmed that surface-mediated oxygen transfer at Mo redox centers is the rate-determining step under these conditions. This modest reduction to $k = 0.05178$ min^{-1} at 15 wt% Mo loading indicates partial aggregation of Mo species, which makes interfacial active site accessibility more difficult and demonstrates a classical structure–activity relationship where optimum catalytic

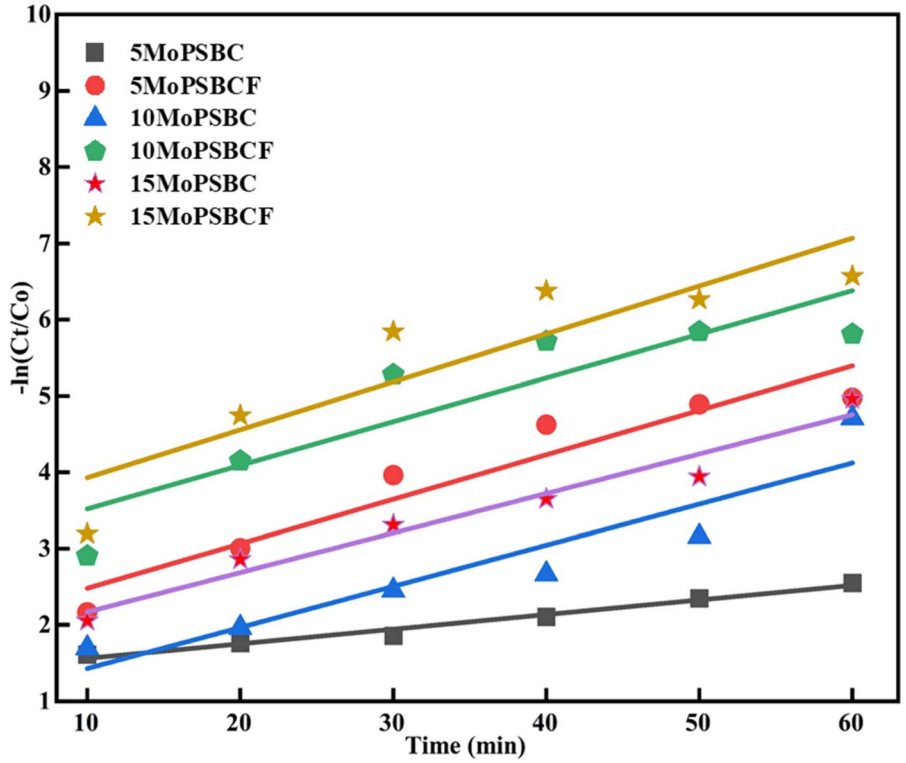

Fig. 11 Pseudo-first-order kinetic plots for the *x*MoPSBC and *x*MoPSBCF catalysts at 5, 10, and 15 wt% Mo loadings.

Table 1 Pseudo-first-order kinetic parameters for DBT removal over the Mo/PSBC and Mo/PSBCF catalysts

Catalyst	k (min^{-1})	Intercept b	R^2
5MoPSBC	0.01918	1.36788	0.9803
5MoPSBCF	0.05826	1.89834	0.9162
10MoPSBC	0.05392	0.88736	0.8723
10MoPSBCF	0.05725	2.94595	0.8137
15MoPSBC	0.05178	1.65086	0.9612
15MoPSBCF	0.06281	3.30093	0.8114

activity is attained at an intermediate metal level and not at the maximum metal level. The strict pseudo-first-order behavior of the reaction is supported by the high R^2 values of 0.9803 and 0.9612 for 5MoPSBC and 15MoPSBC, respectively, across the reaction window under kinetically controlled conditions with limited transport.

The inclusion of formic acid significantly accelerated the reaction, making the catalytic performance insensitive to the MoO_2 loading. The rate constant of 5MoPSBCF (k = 0.05826 min^{-1}) was threefold greater than that of the 5MoPSBC catalyst, which was untouched, and 15MoPSBCF had the highest rate constant with k = 0.06281 min^{-1}. The slightly reduced R^2 values found for the formic acid promoted catalysts (0.811–0.916) are attributed to accelerated kinetics, as opposed to an apparent loss of pseudo-first-order kinetics, as the increased rate of oxidation approaches diffusion-controlled delivery of dibenzothiophene, giving rise to curvature typical of a shift to mass-transfer limitation. Taken together, these findings substantiate the idea that MoPSBC functions through a synergistically heterogeneous-homogeneous oxidation mechanism in which Mo-surface redox cycling and performic-acid co-activation complement each other in the desulfurization process. Therefore, formic acid is proven to be an effective kinetic promoter that offers a feasible and scalable route to the realization of ultra-deep desulfurization under mild, industrially feasible conditions.

3.2.4. Catalytic mechanism. Based on the experimental evidence and consistent with established molybdenum peroxo-chemistry, a coherent multi-step catalytic mechanism is proposed for the first time to the PSBC system, as shown in Fig. 12. The cycle is initiated by the interaction of H_2O_2 with surface-bound Mo^{4+} centers on the monoclinic MoO_2 nanoparticles, generating reactive BC-Mo-OOH hydroperoxo species (Step 1), which are subsequently transformed into highly electrophilic oxoperoxo-molybdenum (Mo^{6+}–O–O) intermediates, which are the principal active species responsible for the oxidation of sulfur compounds.

This activation step is inherently temperature-sensitive, directly rationalizing the pronounced enhancement in catalytic performance observed upon increasing the reaction temperature from 40 °C to 70 °C, as thermal energy effectively lowers the apparent activation barrier for the $Mo^{4+} \rightarrow Mo^{6+}$ oxidation state transition and peroxo-complex stabilization.

At the same time, DBT molecules are sequestered onto the hydrophobic biochar support *via* π–π interactions between the aromatic rings of DBT and the graphitic carbon surface (Step 2), effectively concentrating the sulfur substrate in the immediate

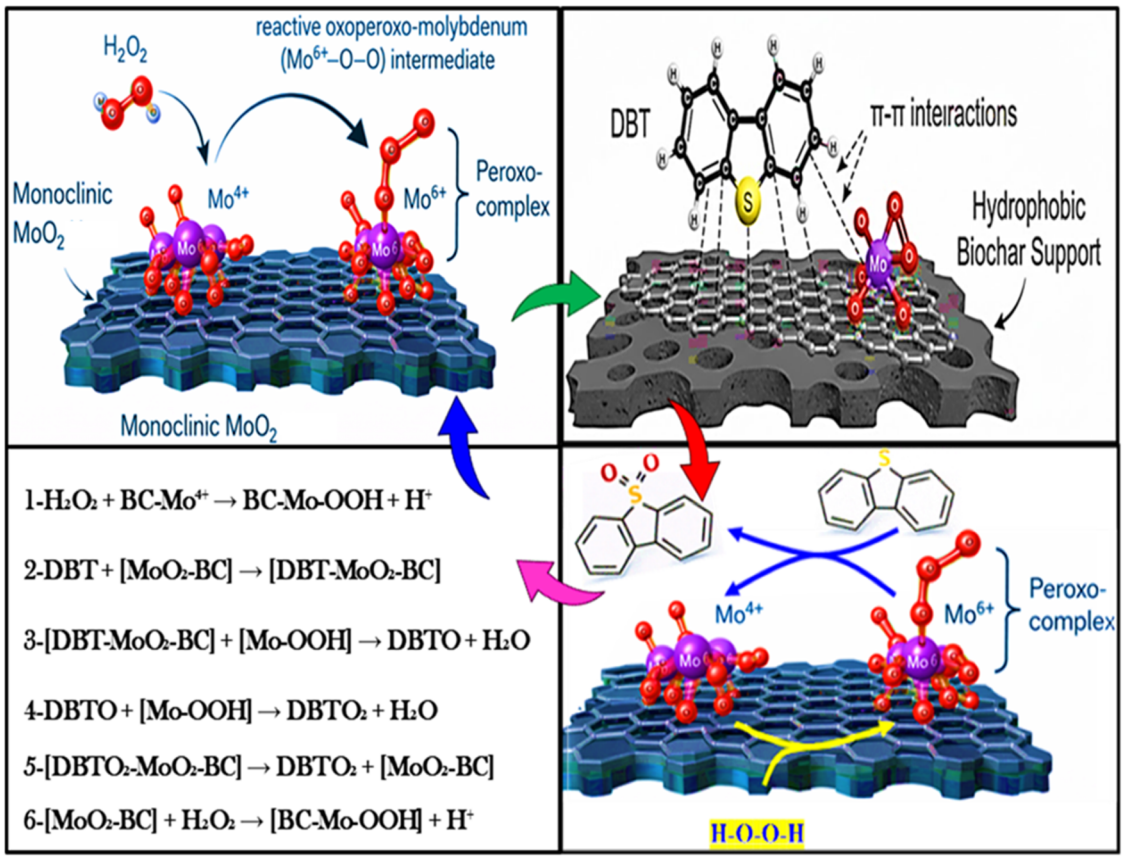

Fig. 12 Proposed oxidative desulfurization mechanism of DBT over MoO_2/biochar *via* the reactive oxoperoxo-Mo intermediates.

proximity to the active Mo atom. This adsorption-facilitated preconcentration mechanism is strongly governed by catalyst dosage: increasing the 15MoPSBC loading to the optimal 0.06 g directly amplifies the density of accessible π–π adsorption sites and Mo–OOH active centers, driving DBT conversion to exceed 99.3%, beyond which additional dosage yields diminishing returns consistent with a transition to a mass-transfer-limited regime. The adsorbed intermediate [DBT-MoO_2-BC] subsequently undergoes sequential and regioselective oxygen transfer from the peroxo species, first yielding DBT sulfoxide (DBTO, Step 3) and subsequently DBT sulfone ($DBTO_2$, Step 4), with water as the byproduct. The catalytic cycle concludes with the desorption of $DBTO_2$ from the catalyst surface and regeneration of Mo^{4+} active centers *via* reoxidation by H_2O_2, thereby closing the redox cycle (Steps 5 and 6). This mechanistic framework is fully consistent with the H_2O_2/S molar ratio optimization data: at H_2O_2/S = 2, insufficient peroxo-intermediate generation limits conversion to 93.0–95.3%, whereas at the optimal H_2O_2/S = 6, complete saturation of Mo active sites with reactive oxygen atoms drives the reaction to near-completion, exceeding 99.1%.

Lastly, the introduction of formic acid superimposes a synergistic dual homogeneous–heterogeneous oxidation pathway through the *in situ* generation of performic acid, which simultaneously stabilizes electrophilic peroxo molybdenum intermediates and generates additional reactive oxygen species capable of oxidizing sterically hindered sulfur compounds that are resistant to the heterogeneous pathway alone. This chemical promotion strategy accounts for the dramatic kinetic acceleration observed in the MoPSBCF systems and their exceptional resilience in real diesel fuel matrices, where 10MoPSBCF achieved 94.6% sulfur removal, reducing the initial sulfur content from 1715 ppm to approximately 89 ppm, firmly establishing the MoPSBC platform as a stable and commercially viable candidate for next-generation deep-desulfurization technologies.

4 Conclusion

This work establishes that controlled carbothermal reduction of PSBC is a robust strategy for stabilizing phase-pure monoclinic MoO_2 nanoparticles within a well-developed carbonaceous scaffold, as unambiguously confirmed by SEM, EDX, XRD, FTIR, and DSC characterization. The 10 wt% loading of Mo as the optimum structural parameter is independently determined by DSC thermal analyses, kinetic analysis, and catalytic performance analysis; additional loading results in premature aggregation, which reduces the availability of interfacial active sites.

Under the optimized conditions (70 °C, O/S = 6, and 60 min), the 15MoPSBC formulation was able to achieve near-complete conversion of DBT (>99.3%) using a high concentration model fuel, and the formic acid-promoted 10MoPSBCF formulation

decreased the real gas oil sulfur content from 1715 ppm L^{-1} to about 89 ppm L^{-1} (94.6%). This catalytic activity is mechanistically assisted by a reversible redox Mo^{4+}/Mo^{6+} cycle that produces electrophilic oxoperoxo intermediates that are synergistically paired with π–π stacking mediated DBT preconcentration on the graphitic biochar surface. The presence of this dual-function adsorption-oxidation mechanism can be supported by pseudo-first-order kinetics as well as by the fact that the rate of reaction increased threefold with the addition of formic acid.

Overall, these findings demonstrate that waste biomass valorization and advanced fuel purification are mutually reinforcing objectives that can be achieved within a single sustainable catalytic framework, positioning MoPSBC as a promising candidate for next-generation deep-desulfurization technologies.

Conflicts of interest

There are no conflicts of interest to declare.

Data availability

The data that support the findings of this study are available from the corresponding author upon reasonable request.

References

1 V. Chandra Srivastava, An evaluation of desulfurization technologies for sulfur removal from liquid fuels, *RSC Adv.*, 2012, **2**, 759–783.
2 R. Javadli and A. de Klerk, Desulfurization of heavy oil, *Appl. Petrochem. Res.*, 2012, **1**, 3–19.
3 J. M. Moradian, *et al.*, Sensors Innovations for Smart Lithium - Based Batteries : Advancements , Opportunities , and Potential Challenges Charge Coupled Device, *Nano-Micro Lett.*, 2025, **17**, 1–80.
4 A. Naveed, *et al.*, Revisiting recent and traditional strategies for surface protection of Zn metal anode, *J. Power Sources*, 2022, **525**, 231122.
5 C. Song, An overview of new approaches to deep desulfurization for ultra-clean gasoline, diesel fuel and jet fuel, *Catal. Today*, 2003, **86**, 211–263.
6 I. V. Babich and J. A. Moulijn, Science and technology of novel processes for deep desulfurization of oil refinery streams: A review, *Fuel*, 2003, **82**, 607–631.
7 W. Zhu, G. Zhu, L. Huaming, C. Yanhong, Y. Chang, G. Chen and C. Han, Oxidative desulfurization of fuel catalyzed by metal-based surfactant-type ionic liquids, *J. Mol. Catal. A: Chem.*, 2011, **347**, 8–14.
8 A. Stanislaus, A. Marafi and M. S. Rana, Recent advances in the science and technology of ultra low sulfur diesel (ULSD) production, *Catal. Today*, 2010, **153**, 1–68.
9 Z. Ismagilov, S. Yashnik, M. Kerzhentsev, V. Parmon, A. Bourane, F. M. Al-Shahrani, A. A. Hajji and O. R. Koseoglu, Oxidative desulfurization of hydrocarbon fuels, *Catal. Rev. – Sci. Eng.*, 2011, **53**, 199–255.
10 X. Ma, A. Zhou and C. Song, A novel method for oxidative desulfurization of liquid hydrocarbon fuels based on catalytic oxidation using molecular oxygen coupled with selective adsorption, *Catal. Today*, 2007, **123**, 276–284.
11 B. S. Ahmed, *et al.*, Desulfurization of light and heavy gas oil from crudes of Kurdistan region-Iraq by oxidation and solvent extraction, *J. Sulfur Chem.*, 2025, **46**, 324–344.
12 L. C. Caero, E. Hernández, F. Pedraza and F. Murrieta, Oxidative desulfurization of synthetic diesel using supported catalysts: Part I. Study of the operation conditions with a vanadium oxide based catalyst, *Catal. Today*, 2005, **107–108**, 564–569.
13 A. F. Zwain, Z. M. Shakor and B. Y. Al-zaidi, A Brief Review of the Latest Developments in Hydro-Desulfurization Catalysts Based on Transition Metal Sulfides for the Generation of Diesel with an Extremely Low Level of Sulfur Content, *J. Chem. Soc. Pak.*, 2025, **47**, 66–90.
14 L. Qiu, *et al.*, Oxidative desulfurization of dibenzothiophene using a catalyst of molybdenum supported on modified medicinal stone, *RSC Adv.*, 2016, **6**, 17036–17045.
15 M. A. Rezvani, M. Shaterian, F. Akbarzadeh and S. Khandan, Deep oxidative desulfurization of gasoline induced by PMoCu@$MgCu_2O_4$-PVA composite as a high-performance heterogeneous nanocatalyst, *Chem. Eng. J.*, 2018, **333**, 537–544.
16 D. Wang, *et al.*, Oxidative desulfurization of fuel oil: Part I. Oxidation of dibenzothiophenes using tert-butyl hydroperoxide, *Appl. Catal., A*, 2003, **253**, 91–99.
17 J. M. Campos-Martin, M. C. Capel-Sanchez, P. Perez-Presas and J. L. G. Fierro, Oxidative Processes of Desulfurization of Liquid Fuels, *J. Chem. Technol. Biotechnol.*, 2010, **85**, 879–890.
18 W. Zhu, *et al.*, Oxidative desulfurization of fuels catalyzed by peroxotungsten and peroxomolybdenum complexes in ionic liquids, *Energy Fuels*, 2007, **21**, 2514–2516.
19 B. S. Ahmed, *et al.*, Efficient Oxidative Desulfurization of High-Sulfur Diesel via Peroxide Oxidation Using Citric , Pimelic , and α -Ketoglutaric Acids, *Separations*, 2023, **10**(3), 206.
20 F. F. Roman, J. L. D. D. Tuesta, M. T. Silva, J. L. Faria and H. T. Gomes, Carbon-Based Materials for Oxidative Desulfurization and Denitrogenation of Fuels : A Review, *Catalysis*, 2021, **11**, 1–41.
21 M. Te, C. Fairbridge and Z. Ring, Oxidation reactivities of dibenzothiophenes in polyoxometalate/H_2O_2 and formic acid/H_2O_2 systems, *Appl. Catal., A*, 2001, **219**, 267–280.
22 S. Murata, K. Murata, K. Kidena and M. Nomura, A novel oxidative desulfurization system for diesel fuels with molecular oxygen in the presence of cobalt catalysts and aldehydes, *Energy Fuels*, 2004, **18**, 116–121.
23 Z. S. Gano, F. S. Mjalli, T. Al-wahaibi and Y. Al-wahaibi, Desulfurization of liquid fuel via extraction with imidazole-containing deep eutectic solvent, *Green Process. Synth.*, 2017, **6**, 511–521.
24 H. Fakhri, M. H. Firooz, A. Moteallemi and A. Esrafili, Development and optimization of organic frameworks for

efficient removal of sulfur and nitrogen compounds from diesel fuel under visible light, *Sci. Rep.*, 2026, **16**, 1–12.
25 H. A. Mohammed, H. Y. Mostafa, D. M. Abd, E. Aty and A. M. Ashmawy, Novel Gemini ionic liquid for oxidative desulfurization of gas oil, *Sci. Rep.*, 2023, 1–13, DOI: 10.1038/s41598-023-32539-y.
26 M. Lu, *et al.*, International Journal of Green Energy The Oxidative Desulfurization of Fuels with a Transition Metal Catalyst : A Comparative Assessment of Different Mixing Techniques, *Int. J. Green Energy*, 2014, **11**, 37–41.
27 R. Fu, Y. Zha, C. Huang, Q. Wang and Z. Xiong, Metal-organic frameworks in adsorption desulfurization : Recent progress , new trends and future perspectives, *Coord. Chem. Rev.*, 2026, **548**, 217185.
28 C. Li, *et al.*, Ultra-Deep Desulfurization of Diesel: Oxidation with a Recoverable Catalyst Assembled in Emulsion, *Chem.–Eur. J.*, 2004, **10**, 2277–2280.
29 C. Komintarachat and W. Trakarnpruk, Oxidative desulfurization using polyoxometalates, *Ind. Eng. Chem. Res.*, 2006, **45**, 1853–1856.
30 H. Yang, *et al.*, Heterogeneous oxidative desulfurization of diesel fuel catalyzed by mesoporous polyoxometallate-based polymeric hybrid, *J. Hazard. Mater.*, 2017, **333**, 63–72.
31 M. Zhang, *et al.*, One-pot synthesis, characterization and desulfurization of functional mesoporous W-MCM-41 from POM-based ionic liquids, *Chem. Eng. J.*, 2014, **243**, 386–393.
32 L. Chen, Z. Hu, J. Ren, Z. Wang and Z. Yuan, Microporous and Mesoporous Materials Efficient oxidative desulfurization over highly dispersed molybdenum oxides supported on mesoporous titanium phosphonates, *Microporous Mesoporous Mater.*, 2021, **315**, 110921.
33 A. Afshar and S. Bandehali, A review paper : Recent advance catalysts for desulfurization of fuel oil by ODS technology, *J. Ind. Eng. Chem.*, 2025, **147**, 85–103.
34 Y. Chen, Q. Tian, Y. Tian, J. Cui and G. Wang, Ultra-Deep Oxidative Desulfurization of Fuel with H_2O_2 Catalyzed by Mesoporous Silica-Supported Molybdenum Oxide Modified by Ce, *Appl. Sci.*, 2021, **11**(5), 2018.
35 K. Abdelkader-fern, R. Matos, D. M. Fernandes and A. F. Peixoto, Metal-Supported Biochar Catalysts for Sustainable Biorefinery, Electrocatalysis, and Energy Storage Applications: A Review, *Catalysis*, 2022, **12**, 1–66.
36 W. J. Liu, H. Jiang and H. Q. Yu, Development of Biochar-Based Functional Materials: Toward a Sustainable Platform Carbon Material, *Chem. Rev.*, 2015, **115**, 12251–12285.
37 J. Wang and S. Wang, Preparation, modification and environmental application of biochar: A review, *J. Cleaner Prod.*, 2019, **227**, 1002–1022.
38 D. Bryan, Synthesis Methods, Properties, and Modifications of Biochar-Based Materials for Wastewater Treatment: A Review, *Resourse*, 2024, **13**(1), 8.
39 K. Qian, A. Kumar, H. Zhang, D. Bellmer and R. Huhnke, Recent advances in utilization of biochar, *Renewable Sustainable Energy Rev.*, 2015, **42**, 1055–1064.
40 M. B. Ahmed, J. L. Zhou, H. H. Ngo, W. Guo and M. Chen, Progress in the preparation and application of modified biochar for improved contaminant removal from water and wastewater, *Bioresour. Technol.*, 2016, **214**, 836–851.
41 T. Xie, K. R. Reddy, C. Wang, E. Yargicoglu and K. Spokas, Characteristics and applications of biochar for environmental remediation: A review, *Crit. Rev. Environ. Sci. Technol.*, 2015, **45**, 939–969.
42 P. F. Sherin*et al.*, Preparation And Characterisation Of Biochar From Banana Stem For Removal Of Methylene Blue, *The International Conference on Emerging Trends in Engineering Yukthi*, 2023, pp. 244–248.
43 L. Jing, P. Li, Z. Li, D. Ma and J. Hu, Chem Soc Rev photocatalytic materials and their performance, *Chem. Soc. Rev.*, 2025, 2054–2090, DOI: 10.1039/d4cs00029c.
44 A. Tanimu and K. Alhooshani, Advanced hydrodesulfurization catalysts : A review of design and synthesis, *Energy Fuels*, 2019, **33**, 2810–2838.
45 X. Liang, T. Zhang, H. Yu, J. Hong and M. Abbas, Control of dual-function amphiphilic biochar-MoO_{3-x} catalysts with abundant oxygen vacancies for ef fi cient extractant-free oxidative desulfurization, *Pet. Sci.*, 2025, **22**, 2215–2232.
46 B. Milling, Aerobic Oxidative Desulfurization by Supported Polyoxometalate Ionic Liquid Hybrid Materials via Facile Ball Milling, *Molecules*, 2024, **29**, 1–13.
47 X. He, *et al.*, The effects of H_2O_2 - and HNO_3/H_2SO_4 -modified biochars on the resistance of acid paddy soil to acidification, *Environ. Pollut.*, 2022, **293**, 118588.
48 M. H. Morcali, B. Zeytuncu and O. Yucel, Platinum Uptake from Chloride Solutions Using Biosorbents 2 . Material and Methods, *Mater. Res.*, 2013, **16**, 528–538.
49 Y. Ngernyen, D. Petsri and K. Sribanthao, RSC Advances drug (ibuprofen) onto biochar and magnetic biochar prepared from chrysanthemum waste of, *RSC Adv.*, 2023, **13**, 14712–14728.
50 B. S. Ahmed, *et al.*, Oxidative Desulfurization of Real High-Sulfur Diesel Using Dicarboxylic Acid/H_2O_2 System, *Processes*, 2022, **10**, 206.
51 K. Açıkalın, F. Karaca and E. Bolat, Pyrolysis of pistachio shell : Effects of pyrolysis conditions and analysis of products, *Fuel*, 2012, **95**, 169–177.
52 Z. Khoshraftar and A. Ghaemi, Current Research in Green and Sustainable Chemistry Evaluation of pistachio shells as solid wastes to produce activated carbon for CO_2 capture : Isotherm , response surface methodology (RSM) and arti fi cial neural network (ANN) modeling, *Curr. Res. Green Sustainable Chem.*, 2022, **5**, 100342.
53 M. Konsolakis, N. Kaklidis and G. E. Marnellos, Assessment of biochar as feedstock in a direct carbon solid oxide fuel cell, *RSC Adv.*, 2015, **5**, 73399–73409.
54 P. Balasundara, P. Narayanasamy, S. Senthil, R. Naif Abdullah Al-Dhabi, R. Prithivirajan, T. Shyam Kumare and K. S. B. Ramkumar, Physico-Chemical study of Pistachio (Pistacia vera) Nutshell particles as a Bio-filler for Eco-friendly Composites, *Mater. Res. Express*, 2019, **6**, 27.
55 K. A. Komnitsas and D. Zaharaki, Morphology of Modified Biochar and Its Potential for Phenol Removal from Aqueous Solutions, *Front. Environ. Sci.*, 2016, **4**, 1–11.

56 W. Yang, Q. Chen and M. Qiu, The synthesis of PEG/MoS_2-modified biochar for the efficient removal of Cr(vi) in solution: performance and mechanism, *RSC Adv.*, 2025, **15**, 46967–46980.

57 L. Garcı, G. A. Fuentes, M. E. Herna, F. Murrieta-guevara and F. Jime, Ultra-deep oxidative desulfurization of diesel fuel by the Mo/Al_2O_3-H_2O_2 system : The effect of system parameters on catalytic activity, *Appl. Catal., A*, 2008, **334**, 366–373.

58 S. A. Abdulhadi and H. H. Alwan, South African Journal of Chemical Engineering Oxidative desulfurization of model fuel using a NiO-MoO_3 catalyst supported by activated carbon : Optimization study, *S. Afr. J. Chem. Eng.*, 2023, **43**, 190–196.

59 J. B. Bhasarkar, S. Chakma and V. S. Moholkar, Ultrasonics Sonochemistry Investigations in physical mechanism of the oxidative desulfurization process assisted simultaneously by phase transfer agent and ultrasound, *Ultrason. Sonochem.*, 2015, **24**, 98–106.

60 W. Ahmad and I. Ahmad, Desulphurization of Transportation Fuels by Per-Formic Acid Oxidant Using MoO x Loaded on ZSM-5 Catalyst, *J. Energy Power Eng.*, 2017, **5**, 87–99.